Journal of Engineering Science and Technology
Vol. 18, No. 3 (2023) 1539 - 1560

ON THE STABILITY OF PULSATILE FLOW IN THE PRESENCE OF A TRANSVERSE MAGNETIC FIELD

ABDALRAZZAQ K. ABBAS[1], ALI A. ABDULRASOOL[1,*], MOHAMMED W. ALJIBORY[1], WAEL N. ABDULLAH[2]

[1]University of Kerbala, College of Engineering, Department of Mechanical Engineering Karbala-56001, Iraq
[2]Mustansiriyah University, College of Engineering, Department of Mechanical Engineering, Baghdad-10047, Iraq
*Corresponding Author: ali.abdulrasool@uokerbala.edu.iq

Abstract

In this paper, an analytical solution of unsteady laminar flow is derived in terms of Hartmann and Womersley numbers with the aim of representing the flow behavior in a magnetic environment. Periodic disturbance growth is assessed using the quasi-steady approach, by which different transition onsets are determined with and without the effect of magnetic field. The new stability curve of the current theory is combined with other significant counterparts from the literature to reach a satisfied prediction. The theoretical results are also verified by the numerical solution of the linearized Navier-Stokes equations showing a good agreement even at relatively high Reynolds and Womersley numbers. They indicate that flow stability can only be improved at low-frequency flow oscillation by increasing the magnetic effect. The flow appears to be undisturbed in the magnetized medium at one neutral point if the Womersley number remains constant. In addition, two-dimensional direct numerical simulations (DNS) for smooth and rough pipe flows are performed. The computational data confirms the linear stability results and shows that area reduction and roughness along the flow path, as well as magnetization at high Womersley numbers, have the greatest influence on flow.

Keywords: Constricted pipe, Linear stability theory (quasi-steady), Magnetic field effect, Transition onsets, Two-dimensional simulation (2D), Unsteady pulsatile flow, Wall roughness.

1. Introduction

Pulsatile flows are natural phenomena and common in fluid dynamics, where the oscillatory component is superimposed on a steady base. This kind of flow has been mostly analysed for its transition to turbulence in different geometries. However, since the velocity measurement in pulsating flows is more difficult than that in steady flows [1] and all other setup conditions of conducting an experiment, the transition process is not fully covered, and still to be in the presence of external factors such as the magnetic field.

The pulsatile pressure gradient causes wall shear stress to oscillate with time [2]. Misra and Shit [2] and Parida [3] introduced an investigation for the effect of a uniform magnetic field on the distribution of velocity and other quantities. A theoretical study carried out by Sharma et al. [5] was implemented on the constricted flow domain only and found that the wall shear stress increases as the magnetic field increases. The study of Khechiba et al. [6] reached an analytical solution to express the relation among Hartmann number, Darcy number (the relation between the permeability of the medium and its cross-sectional area) and the stress coefficient for the pulsating pipe flow with porous medium. The Hartmann number is the ratio of electromagnetic force to the viscous force, or $Ha = B^* R^* \sqrt{\sigma^* / \mu^*}$. The magnetic field is B^*, the pipe radius is R^*, electrical conductivity is σ^*, and $\mu^*$is the dynamic viscosity. The findings showed that the permeability parameter of medium and the Hartmann number (Ha) significantly influence the flow behavior.

Camobreco et al. [7] introduced an investigation on liquid metal coolant ducts subjected to transverse magnetic field. A steady pressure gradient and simultaneous oscillation of the lateral walls drive the flow. Near the hydrodynamic limit at $H = 10^{-7}$, a nearly 70% drop in the critical Reynolds number was obtained, compared to that for the steady base flow, while $H = 10$ yielded slightly over a 90% reduction, where $H = G\ Ha$ is the friction parameter, and G is the characteristic parameter.

Two-dimensional analysis (stream function-vorticity formulation) was used in Bandyopadhyay and Layek [8]'s study for locally constricted channel flow in the presence of an external transverse uniform magnetic field. The flow separation region shrinks as the magnetic intensity is enhanced, according to their study. When the strength of the magnetic field increases, the axial velocity flattens out. The temporal variations in wall shear stress rise with increasing the magnetic parameter as shown for both steady and pulsatile flow conditions. Kiran et al. [9] evaluated pulsatile flow of dusty fluid through a constricted channel in the presence of a magnetic field. As the magnetic strength becomes higher, the shear stress of the fluid acting on the wall increases, but the pressure drops.

Regarding the linear stability without considering the magnetism, the Floquet theory was employed by Thomas et al. [10] to find the critical Reynolds numbers ($Re = \hat{u}^* R^* / \nu^*$), wavenumbers and pulsation ratios between the oscillating and steady flow amplitudes at a wide range ($1\times10^{-4} < A < 1\times10^{4}$), where A is the pulsation ratio or $\hat{u}_o^* / \hat{u}_s^*$. The results deviate from those of previous experiments in terms of critical Reynolds numbers, which were unpredictable when the pulsation ratio reached unity due to the large number of harmonics needed by the Floquet method for the disturbances representation. The same approach was also used by Sadrizadeh [11] to investigate the modal and non-modal modes for the

Newtonian and non-Newtonian fluids. Based on their linear stability analysis, the flow is asymptotically stable in either configuration, or the pulsatile flow is marginally more stable than the steady flow.

Instead of the Chebyshev basis, the numerical study of Fedele et al. [12] used the Galerkin method to solve the linear stability equation. The results showed that the pulsatile flow is somewhat more stable than the steady flow at wavenumber = 1, the pulsation ratio = 2 and different Womersely numbers ($R^*\sqrt{\Omega^* / \nu^*}$), while the maximum real parts of the eigenvalues were taken. The perturbation energy of disturbances was calculated for a pulsatile channel flow at different flow conditions by Pier and Schmid [13]. The results were consistent with those of the Floquet method for linear stability analysis, albeit the pulsation ratio was crucial in determining the transition thresholds. The direct numerical simulations of Xu and Avila [14] showed that the length of the pipe, disturbance amplitude and the Womersley and Reynolds numbers are behind the discrepancies referring to the correct transition curve in the literature.

Direct numerical simulations of flow stability affected by 75% stenosis (constricted path) were performed by Varghese et al. [15]. The asymmetry was the factor of destabilization the flow. Direct numerical simulations of Sherwin and Blackburn [16] for axisymmetric perturbations with a reduction area of 75% were also performed for steady and pulsatile flows. The same investigators, Sherwin and Blackburn [16], carried out three-dimensional Floquet analysis for a single-harmonic case, and the critical Reynolds numbers were 389, 417 and 500 while the critical Womersley numbers were 15.6, 11.4 and 10.2, respectively, with a pulsation ratio of one.

The transition-turbulence stages were identified experimentally by Xu et al. [17] and categorized according to the Womersely number (α). When α < 2.5, the first stage can be predicted by the quasi-steady assumption (same terminology but stands for a different meaning than the principle of the current theory). The second stage is at $\alpha \geq$12, at which the flow pulsation does not affect the transition onsets. More details were demonstrated in the study Lee and Abdulrasool [18] when the accuracy of the given quasi-steady approach was found valid for all α values. For approximately similar axisymmetric geometries presented in this paper, Griffith et al. [19] had experimentally noticed a vortex ring in the post-stenotic areas varying with the stenosis degree. Also, Griffith et al. [19] observed a higher wall shear stress at a lower pulse time and higher stenosis degree, and the flow was less stable than what the numerical analysis of the Floquet method indicated.

The main purpose of this study resembles that of Xu et al. [17]'s experiment, which demonstrated the stability map of pulsating pipe flows but had no magnetic effect. This includes the domain size, Reynolds and Womersley number ranges, and even the concept of the qausi-steady theory that predicts the transition to turbulence at certain stages throughout one oscillation cycle. The stability of pulsatile pipe flow is investigated below by taking into account a variety of factors such as the magnetism, which has not been considered previously. This analysis for Newtonian incompressible fluid flow undergoing a uniform magnetic field is carried out using the quasi-steady method when the pulsation ratio (A) is one, i.e. $\hat{u}_o^* = \hat{u}_s^*$. This technique deals with the laminar base flow by obtaining the cycle-averaged growth rate of disturbance regardless of the axial location, whereas Xu et al. [17] used the survival probability principle, explained in their study. The validity of the current

results is tested by a direct solution to the time-dependent linearized Navier-Stokes equations and other relevant experiments. In the case of non-linear disturbances, 2D direct numerical simulations are performed for the flow transition following the Abdulrasool [20] 's paradigm. The wall imperfections represented by waviness are introduced to analyse the flow mainly via the behavior of wall shear stress.

2. Governing Equations

For the current analyses, a two-dimensional domain of x and r axes subjected to a time-varying pressure gradient is considered. The flow is laminar inside a flat smooth pipe, while the obstruction and wall irregularity will be incorporated in the transition regime. The flow is exposed to a transverse magnetic field of constant flux density (B^*) and electrical conductivity (σ^*) according to the magnetohydrodynamic (MHD) principle [21]. Thus, the governing equations for such flow with constant physical properties are

$$\frac{1}{r^*}\frac{\partial}{\partial r^*}(r^* v^*) + \frac{\partial u^*}{\partial x^*} = 0, \tag{1}$$

$$\frac{\partial u^*}{\partial t^*} + v^*\frac{\partial u^*}{\partial r^*} + u^*\frac{\partial u^*}{\partial x^*} = -\frac{1}{\rho^*}\frac{\partial p^*}{\partial x^*} - \frac{\sigma^* B^{*2}}{\rho^*}u^* + \nu^*\left\{\frac{1}{r^*}\frac{\partial}{\partial r^*}\left(r^*\frac{\partial u^*}{\partial r^*}\right) + \frac{\partial^2 u^*}{\partial (x^*)^2}\right\}, \tag{2}$$

$$\frac{\partial v^*}{\partial t^*} + v^*\frac{\partial v^*}{\partial r^*} + u^*\frac{\partial v^*}{\partial x^*} = -\frac{1}{\rho^*}\frac{\partial p^*}{\partial r^*} + \nu^*\left\{\frac{1}{r^*}\frac{\partial}{\partial r^*}\left(r^*\frac{\partial v^*}{\partial r^*}\right) + \frac{\partial^2 v^*}{\partial (x^*)^2} - \frac{v^*}{(r^*)^2}\right\}, \tag{3}$$

where the velocity components of u^* and v^* are in the axial and radial directions, respectively. The maximum velocity ($\hat{u}^*$) representing the amplitude of the combined parts ($\hat{u}^* = \hat{u}^*_{steady} + \hat{u}^*_{oscillatory}$) is selected as a main characteristic parameter, and the following non-dimensional variables: $x = x^*/R^*$, $r = r^*/R^*$, $u = u^*/\hat{u}^*$, $p = p^*/\rho\hat{u}^{*2}$, $t = t^*/(R^*/\hat{u}^*)$, $\tilde{\psi}^* = \tilde{\psi}^*/(\hat{u}^*(R^*)^2)$ are employed accordingly. For a fully developed axisymmetric laminar flow with magnetic field being considered, the nondimensionalized form of Eq. (2) yields to

$$\frac{\partial u}{\partial t} = -\frac{\partial p}{\partial x} - \frac{\mathrm{Ha}^2}{\mathrm{Re}}u + \frac{1}{\mathrm{Re}}\left(\frac{\partial^2 u}{\partial r^2} + \frac{1}{r}\frac{\partial u}{\partial r}\right). \tag{4}$$

Equation (4) can be solved analytically, and the solution when Ha= 0 as first introduced by Womersley [22] is

$$U(r,t) = 1 - r^2 + \left|\frac{J_0(\alpha\cdot i^{3/2})}{J_0(\alpha\cdot i^{3/2})-1}\right|\cdot\mathbb{R}\left[\left(1 - \frac{J_0(\alpha\cdot i^{3/2}\cdot r)}{J_0(\alpha\cdot i^{3/2})}\right)\cdot\frac{e^{i\Omega t}}{i}\right], \tag{5}$$

which clearly depends on α (Womersely number or $R^*\sqrt{\Omega^*/\nu^*}$), and $U(r,t)$ is u^* normalized by $\hat{u}^*$ for laminar flow. Herein, the same procedure can be used to convert the linear partial differential equation (Eq. (4)) into a modified Bessel differential equation when > 0 , and the solution can be written as

$$U(r,t) = \left|\frac{I_0(Ha)}{I_0(Ha)-1}\right|\left(1 - \frac{I_0(Ha\cdot r)}{I_0(Ha)}\right) + \left|\frac{I_0(\gamma)}{I_0(\gamma)-1}\right|\cdot\mathbb{R}\left[\left(1 - \frac{I_0(\gamma\cdot r)}{I_0(\gamma)}\right)\cdot\frac{e^{i\Omega t}}{i}\right], \tag{6}$$

where the complex number γ is equivalent to $\sqrt{Ha^2 + i\alpha^2}$. The derivation of Eq. (6) is given in Appendix A. Note that both derived solutions are obtained depending on the fact that the pressure gradient driving the flow is periodic with time or

$-\partial p^*/\partial x^* = \sum_{n=0}^{M} A_n^* e^{i\Omega^* n t^*}$, at which n represents the number of harmonics, and M is theoretically infinite. Equations (2) and (3) can be coupled into one equation by adopting the principle of stream function, where the two velocities, $u^* \equiv \frac{1}{r^*}\frac{\partial \tilde{\psi}^*}{\partial r^*}$ and $v^* \equiv -\frac{1}{r^*}\frac{\partial \tilde{\psi}^*}{\partial x^*}$, satisfy the continuity equation (Eq. (1)). The final form of the combined Eqs. (2) and (3) will be

$$\frac{\partial}{\partial t}(\Delta\tilde{\psi}) - \frac{1}{r}\frac{\partial \tilde{\psi}}{\partial x}\frac{\partial}{\partial r}(\Delta\tilde{\psi}) + \frac{1}{r}\frac{\partial \tilde{\psi}}{\partial r}\frac{\partial}{\partial x}(\Delta\tilde{\psi}) + \frac{2}{r^2}\frac{\partial \tilde{\psi}}{\partial x}(\Delta\tilde{\psi}) = \frac{1}{Re}\Delta(\Delta\tilde{\psi}) + \frac{\mathrm{Ha}^2}{\mathrm{Re}}\left(\frac{\partial^2\tilde{\psi}}{\partial r^2} - \frac{1}{r}\frac{\partial \tilde{\psi}}{\partial r}\right). \quad (7)$$

The linear operator, which is the same as the Laplace operator except the negative sign in the second term, is

$$\Delta \equiv \frac{\partial^2}{\partial (r)^2} - \frac{1}{r}\frac{\partial}{\partial r} + \frac{\partial^2}{\partial (x)^2}.$$

The velocity profiles should be precisely represented when the overshot phenomenon appears, and the pressure gradient can be expressed by the Fourier series. Experimentally, for mass-flow-rate driven flows, where the pressure gradient has to be assumed first and then the derivations are performed, the measurements of pressure gradient are not feasible and reliable, especially in shrinking regions [23]. Thus, some estimations for the pressure drop are often made as done in the study of Ha et al. [24]. It should be noted that these experimental adjustments may have contributed to the disparities in transition onsets, shown later in a figure.

3. Linear Stability

The stability studies devoted for the pulsating flows are noticed to be less than those of the purely oscillating flows. Even the predictions of their transition onsets are not consistent, since in cases where the mean flow contains oscillations, various factors bring extra discrepancies [25]. However, the linear analysis will be revisited here, and their results will be evaluated against those of the most rigorous experiments. To begin with, the decomposition of the stream function which is $\tilde{\psi}(t,r,x) = \Psi(t,r) + \psi(t,r,x)$ can be substituted into the Eq. (7), and the non-linear terms can be terminated. Also, the base flow of U can be incorporated in Eq. (7) via

$$U \equiv \frac{1}{r}\frac{\partial \Psi}{\partial r}, \quad \frac{\partial U}{\partial r} = \frac{1}{r}\Delta\Psi, \quad \frac{\partial^2 U}{\partial r^2} = \frac{1}{r}\left[\frac{\partial}{\partial r}(\Delta\Psi) - \frac{1}{r}\Delta\Psi\right],$$

where $\Delta\Psi \equiv \frac{\partial^2\Psi}{\partial r^2} - \frac{1}{r}\frac{\partial \Psi}{\partial r}$, and the linearized equation is then written as

$$\frac{\partial}{\partial t}(\Delta\psi) = -U\frac{\partial}{\partial x}(\Delta\psi) - \left(\frac{1}{r}\frac{\partial U}{\partial r} - \frac{\partial^2 U}{\partial r^2}\right)\frac{\partial \psi}{\partial x} + \frac{1}{Re}\Delta(\Delta\psi) + \frac{\mathrm{Ha}^2}{\mathrm{Re}}\left(\frac{\partial^2\psi}{\partial r^2} - \frac{1}{r}\frac{\partial \psi}{\partial r}\right). \quad (8)$$

The traveling-wave disturbance is considered, and the stream function for 2D disturbances in the terms of the amplitude (η) and the wavenumber (k) in the axial direction only is assumed with $\psi(t,r,x) = \eta(t,r)e^{ikx}$. If this later form is plugged into the Eq. (8), the linearized equation for disturbances becomes

$$\frac{\partial}{\partial t}L(\eta) = -ik\left\{UL(\eta) + \left(\frac{1}{r}\frac{\partial U}{\partial r} - \frac{\partial^2 U}{\partial r^2}\right)\eta\right\} + \frac{1}{Re}L^2(\eta) + \frac{\mathrm{Ha}^2}{\mathrm{Re}}\left(\frac{\partial^2\eta}{\partial r^2} - \frac{1}{r}\frac{\partial \eta}{\partial r}\right), \quad (9)$$

where $L \equiv \frac{\partial^2}{\partial r^2} - \frac{1}{r}\frac{\partial}{\partial r} - k^2$. The boundary conditions are no-slip at the wall ($\eta = 0$) and bounded velocity at r =0, or$\frac{\partial \eta}{\partial r} = 0$.

3.1. Quasi-Steady Method

The assumption of quasi-steady is applied to the current flow with non-zero mean velocity. It is based on the frozen profiles to the temporal changes of the laminar base flow velocity, as previously tested by Lee and Abdulrasool [18] for purely oscillating flows. Therefore, the amplitude of disturbance function in Eq. (9) is assumed to be

$$\eta(t, r) = \phi(r) \exp\left[-\mathrm{i} \int_0^t \omega(s)\, \mathrm{d}s\right], \tag{10}$$

in terms of the current theory, where ϕ and ω are complex functions. The modified eigenvalue problem can be written as

$$\frac{1}{Re} L^2(\phi) - \mathrm{i}\, k \left\{U\, L(\phi) + \left(\frac{1}{r}\frac{\partial U}{\partial r} - \frac{\partial^2 U}{\partial r^2}\right)\phi\right\} + \frac{\mathrm{Ha}^2}{\mathrm{Re}}\left(\frac{\partial^2 \phi}{\partial r^2} - \frac{1}{r}\frac{\partial \phi}{\partial r}\right) = \lambda L(\phi), \tag{11}$$

where $\lambda = -\mathrm{i}\omega$ and $c \equiv \omega/k$. The parameter c is a complex eigenvalue and represents the wave velocity scaled by $\hat{u}^*$, and ϕ is a complex eigenfunction nondimensionalized by $\hat{u}^* \cdot (R^*)^2$. This type of linear stability is temporal, involving the evolution of disturbances with time. The pulsation ratio (A) was taken unity, so that the peak of the oscillating velocity component is equal to that of the steady flow. The symmetric eigenvalue problem of Eq. (11) was solved by a built-in Matlab routine, and the maximum eigenvalues and eigenfunctions were considered only for the analyses. For spatial discretization, Chebyshev collocation derivatives of [0 , R] domain were used. The numerical accuracy of these derivatives were verified at different numbers of collocation points, where eventually the total of 61 points was determined to be adequate.

3.2. Linearized Navier-Stokes equations

To validate the findings of the present theory (quasi-steady method), Eq. (9) was solved numerically. This initial value equation was formed using Chebyshev collocation derivatives, the same as those used for Eq. (11), and the 4th-order Runge-Kutta method was chosen for the time advancement. It is known that the global accuracy of the spectral method can be maintained if the time step is sufficiently small. Herein, the choice of $\Delta t = \pi * 10^{-5}$ was found to be sufficient for Eq. (9). The linearized equation was rearranged as a matrix,

$$\frac{d\eta}{dt} = M(t)\eta, \tag{12}$$

where

$$M(t) = L^{-1}\left[-\mathrm{i}k\left(UL + \frac{1}{r}\frac{\partial U}{\partial r} - \frac{\partial^2 U}{\partial r^2}\right)\right] + L^{-1}\left[\frac{1}{Re}L^2 + \frac{\mathrm{Ha}^2}{\mathrm{Re}}\left(\frac{\partial^2 \eta}{\partial r^2} - \frac{1}{r}\frac{\partial \eta}{\partial r}\right)\right]. \tag{13}$$

The singularity in Eq. (13) disappeared by applying the boundary conditions of η, which are homogeneous at r = [0, 1]. The first and last rows of matrices in the system of Eq. (12) were replaced by zeros since they are multiplied by the values of η at the boundaries. The solution of Eq. (12) is

$$\eta(m+1) = \eta(m) + \Delta t \sum_{i=1}^{s} b_i h_i, \tag{14}$$

where $h_i = f\left(t_m + w_i\Delta t, \eta_m + \Delta t \sum_{j=1}^{s} a_{ij}h_j\right)$, which is a series function (f) of a number of iterations (m) for the solution η with a time step (Δt). Equation (14) is shown as in Hairer et al. [26], but it can be written in different forms. The parameter s stands for the number of Runge-Kutta stages. Constants b_i and a_{ij} are real numbers whereas $w_i = \sum_{j=1}^{s} a_{ij}$. The norm of the solution is taken to Eq. (12) at different time steps. The growth rates of disturbance were calculated using the following equation, as reported by Singer et al. [27]:

$$GR = \frac{1}{\eta(r,t)}\frac{d\eta(r,t)}{dt}. \quad (15)$$

4. DNS of Transitional Flows

4.1. Blockage and wall roughness

Based on the spectral element approach (SEM), Nek5000 was utilized to accurately represent the flow undergoing the magnetic field and wall roughness. Several researchers have employed this code for both transitional and turbulent flows such as Fischer et al. [28]. The numerical scheme is a Lagrange polynomial of the order $5 \leq N \leq 15$ based on Gauss-Lobatto-Legendre (GLL) points for the velocity and Gauss-Legendre quadrature points for the pressure. The temporal discretization of Eq. (2) is divided into viscous terms treated implicitly by a third-order backward differentiation (BDF3) and non-linear terms solved explicitly by a third-order extrapolation (EXT3). A corrugated surface was built according to the following equation along the x-direction parallel to the wall:

$$f_1(r,x) = r\left[1 + \varepsilon\sin(\frac{2\pi x}{\iota})\right]. \quad (16)$$

Despite the fact that the domain is 2D and overset meshes are not required, the roughness representation is deemed appropriate according to Abdulrasool and Lee [29]. The axisymmetric throat equation at $x = 0$ with a reduced area of 75% is

$$f_2(r,x) = r[1 - \delta(1 + \cos(\pi x))], \quad (17)$$

which is slightly different than that shown in the study of Varghese et al. [15]. The parameter ε is equal to ε^*/R^*, and δ is the blockage amplitude non-dimensionalized by R^*. Equations (16) and (17) were executed in the user-defined routine provided by NEK5000 modifying the shape of the outer mesh as a wavy wall, which has smooth peaks and variable lengths depending on GLL point distributions along the x-coordinate. The ε, ι and δ values are 1%, 50% and 25%, respectively, resulting in 36 roughness elements throughout the pipe. This blockage is located at a distance of $6R$ apart from the inlet. The non-slip boundary conditions are taken at the wall and axisymmetry in the center. The exact velocity solution represented by either Eq. (5) or Eq. (6) is used at the computational inlet condition. The outflow is identified to be a static pressure, and a special treatment to prevent the negative artificial outflow flux from occurring at the end of the pipe is applied [15].

4.2. Mesh convergence

The adequacy of meshing density was evaluated for the current computational domain with a diameter D and length $18D$ via changing the Lagrange polynomial degree (N) only. This was relied on a prior study of Abdulrasool and Lee [29],

where the number of elements was assessed and determined to be suitable for the transition regime. The root-mean-square (RMS) velocities were taken into account for the grid convergence in addition to the velocity residuals in terms of time step as shown in Fig. 1. The mesh independence was examined at $N = 8,10$ and 12 (95.3% and 73% increase, respectively) for a number of elements, or $E = 300$, at the highest Re presented in the DNS work. The total number of elements (E) of $25 \times 12 \times N^2$ for the x-axis, y-axis and polynomial degree, respectively, with clustered mesh cells near the wall was then doubled. The results encountered a maximum relative error of around 8% between the RMS velocities. The normalized residual of the velocity vector, or $\Re(u) = f(u) - \tilde{f}(u)$ where $\Re$ is defined as a local measure of error between the solution $\tilde{f}$ and the exact solution (f) for the entire domain, was approximately between 2.2 to 2.4×10^{-4} over each time step for the two highest resolutions. The time step was chosen to be variable and was initialized at 10^{-3} sec, while the CFL number was fixed at 0.05. DNS results were recorded at every 100 time steps for two consecutive oscillation cycles.

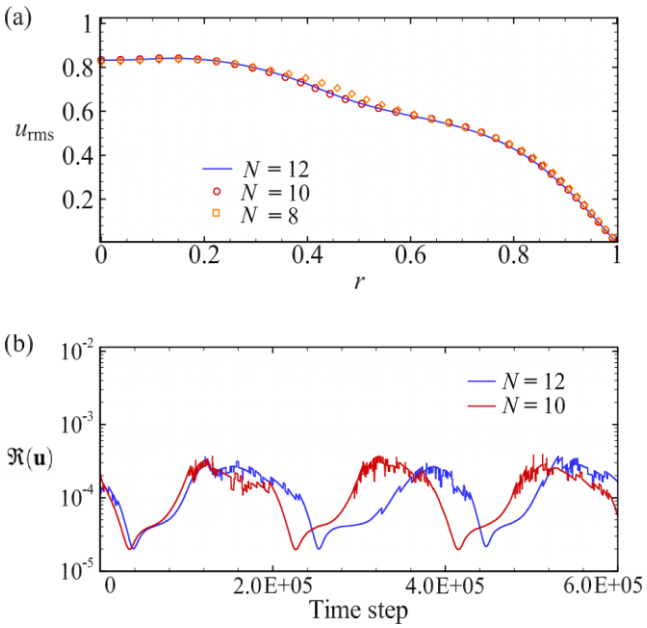

Fig. 1. Mesh independence tests for a 2D-flat smooth pipe with $E = 300$ at $Re = 2500$ and $\alpha = 42.5$ as per: (a) RMS velocity and (b) normalized residual.

5. Results and Discussion

5.1. Axial velocity distribution

The normalized axial velocities obtained from Eq. (6) are shown in Fig. 2 for four Hartmann numbers $(0, 2.5, 5$ and $7)$. The figure demonstrates t/T = 0 and $1/4$ velocity fields for Ha less than 7 with Re = 1200 and α = 28.29. When $Ha = 0$, the flow behaves exactly like the velocity of Womersley (Eq. (5)). The Richardson's annular effect may be seen clearly in the area adjacent to the wall.

This phenomenon becomes more apparent as α increases; in contrast, if α= 0, the velocity profile resembles that of Poiseuille flow. The flow is influenced by the magnetic field in a similar way to how Lorentz force velocimetry works. When a conducting fluid passes through a magnetic field, the flow is dampened and flattens at the center.

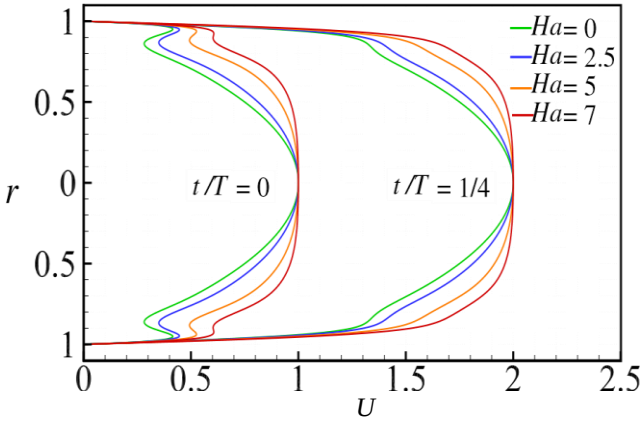

Fig. 2. Normalized axial velocity (U) in the middle of 2D-flat smooth pipe at various Hartmann numbers with Reynolds number ($\mathbf{Re}$) $=$ $\mathbf{1200}$, Womersley number ($\boldsymbol{\alpha}$) $=$ $\mathbf{28.29}$, and pulsation ratio ($\boldsymbol{A}$) $=$ $\mathbf{1}$.

5.2. Wall shear stress (WSS)

In oscillating pipe flow with irregular internal surfaces, there are different techniques for measuring the wall shear stress (τ_w). The experimental measurements of Bauer et al. [30] showed that the Magnetic Resonance Velocimetry (MRV) can be properly used to predict the wall shear stress for both laminar and disturbed flows, whether triggered by the wall irregularity or entrance effects. The amount of WSS is critical because it is higher in the pipe with constricted area than in the pipe without it. The wall shear stress of $\tau_w = \mu\frac{\partial u}{\partial y}$ was used in Fig. 3 to show some magnetic influences, since the fluid was treated Newtonian.

The centreline velocity is plotted in Fig. 3(a) to illustrate the phase change against the wall shear stress. Without the magnetic effect, the figure confirms that τ_w is directly proportional to the frequency of pulses with a big change from α = 7.5 to 42.5, as in the occasions of rapid oscillations. On the other hand, Fig. 3(b) shows a small increase in the wall shear stress at constant Reynolds number (Re) $=$ 1200 and Womersley number (α) $=$ 28.29. The wall shear stress is enhanced because the velocity gradient at the wall grows due to the magnetic influence. As a result, the magnetic field adds to the already high wall shear stresses that occur when the flow area changes, as in a throat. Note that the current study declares that the flow to be laminar at (Re) =1200, Womersley number (α) $=$ 28.29 and Hartmann number (Ha) $=$ 0, but higher Ha changes the flow regime if the other two numbers stay the same.

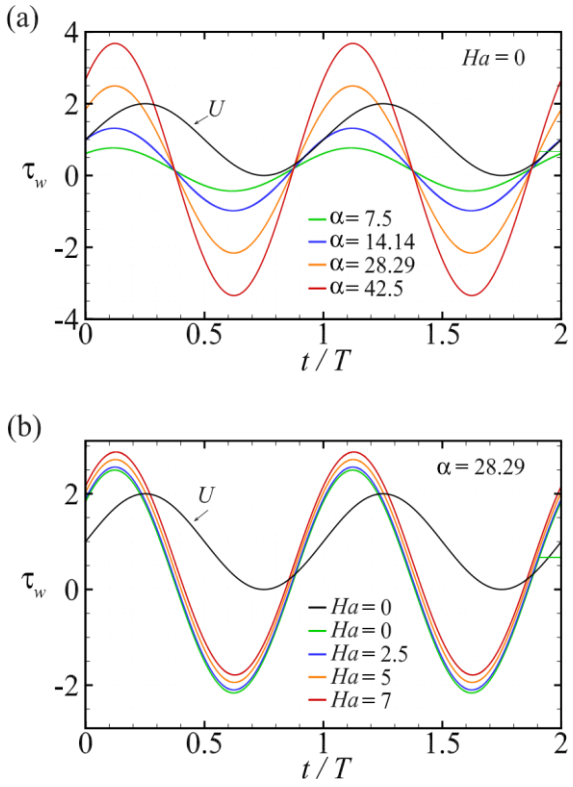

Fig. 3. Analytical solutions of wall shear stress scaled by 0.1 during two oscillation cycles for Reynolds number $(\mathbf{Re}) = 1200$ and pulsation ratio $(A) = 1$ with: (a) Womersley numbers at $Ha = 0$ and (b) Hartmann numbers at α = 28.29.

5.3. Disturbance growth rates

Disturbance growth rates were estimated using the quasi-steady method, considering the maximum imaginary parts of eigenvalue alone ($\mathrm{Im}[\omega]$). Their corresponding eigenfunctions were entered as initial conditions for Eq. (12). For verification purposes, the growth rates (GR) were also obtained using Eq. (12). As shown in Fig. 4, the relation between the two methods was evaluated at $\alpha = 28.29$ and three separate Reynolds numbers $(1265, 2500$ and $5000)$. The patterns of Figs. 4(a) and (b) are qualitatively close, implying similar stability predictions under these flow conditions. The growth rate values are all negative at $Re = 1265$ for long-term oscillation, indicating that the flow is stable. Other flow conditions at Re = 2500 and 5000 cause positive growth rates representing the process leading to turbulence when the flow reverses at three parts of the cycle. Note that t/T in the figure is the phase time of the loop and does not represent the initial time at t = 0. The small discrepancies between the two solutions are due to certain numerical errors created by the ordinary differential equation solver (MATLAB code, used for the temporal discretization of Eq. (14)).

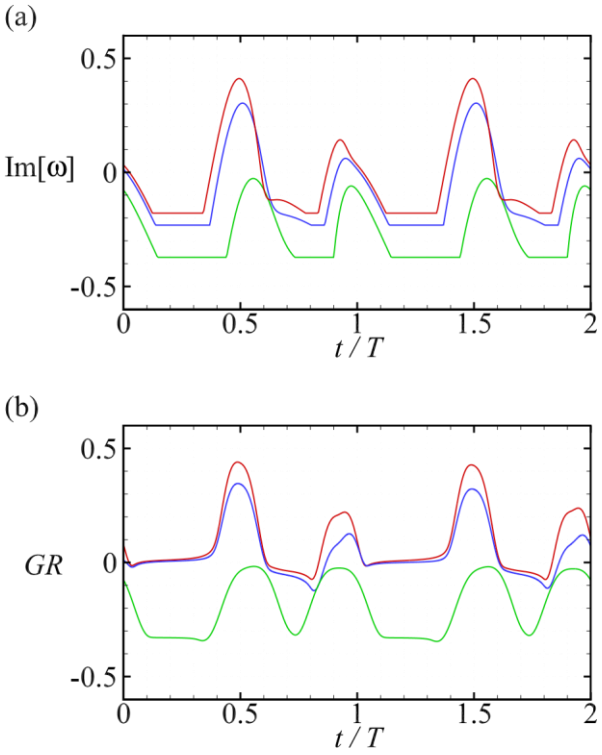

Fig. 4. Growth rates of disturbance calculated by the: (a) presented quasi-steady method and (b) Eq. (15) of linearized Navier-Stokes equations solution scaled by 0.1. The flow conditions are $Ha = 0, \alpha = 28.29, k = 8$ and $Re = 1265$ (green line), 2500 (blue line) and 5000 (red line).

Moreover, since the definition of the growth rate in Eq. (15) varies from that of the quasi-steady method ($\mathrm{Im}[\omega]$), the values shown in Fig. 4(b) have been rescaled so that the growth rate amplitudes at the highest Reynolds numbers become compatible. In the study of Lee and Abdulrasool [18], where the accuracy of quasi-steady method increases with the Reynolds number and Stokes number, or $\alpha/\sqrt{2}$, the results of $\mathrm{Im}[\omega]$ are sufficient to find the critical Reynolds number for a variety of flow conditions. The neutral stability curves were also produced in terms of critical Reynolds number, Womersley number and wavenumber in the same study of Lee and Abdulrasool [18]. The most unstable wave number (k) is discovered to be around 8 at $\alpha = 28.29$ and$1265 \leq Re \leq 2500$. It was found by Abdulrasool [20] that the flow in 2D and 3D domains begins to destabilize at very similar minimum critical Reynolds numbers, verifying the current results for 2D analysis too.

5.4. Critical Reynolds number ($\mathbf{Re_c}$)

According to the literature, there are various aspects involved in estimating the transition thresholds, as well as contradictions in prior studies addressing the transition process for pulsatile flows. In the current case, the onset of transition is thus defined by two regimes, laminar and turbulent, rather than four [31]. The most common data in the literature are included in Fig. 5 with respect to the stability map

of the pulsating flows and shown by different symbols along with those generated with the aid of the current theory.

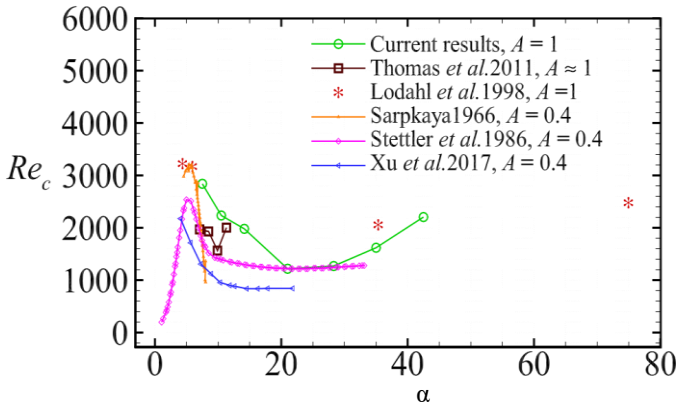

Fig. 5. Critical Reynolds number with Womersley number curves are obtained from the current results (green) predicted by the quasi-steady method, the Floquet theory (brown) by Thomas et al. [10], and others belonging to the famous experiments in the literature.

It can be seen from the figure that the pulsation ratio (A) plays a crucial role as the importance of the Womersley number (α). Increasing the wave-dominated flow, or ≥ 1, will stabilize the flow if the oscillatory component is in the laminar regime, as stated in the analysis of Lodahal et al. [32]. Also, it seems there is a vital zone between α = 5 and 10, where the flow changes its reaction to the disturbances. Since that zone and $A < 1$, the critical Reynolds numbers tend to be constant. In comparison, the stability curves take another trend under other conditions, such as those related to the quasi-steady approach (current study), Floquet theory of Thomas et al. [10] and the experiment of Lodahal et al. [32]. The definition of stability is the most evident cause of these significant differences in stability curves. Since the transition from the laminar to the turbulence regime occurs in stages, some define the first stage as the onset of turbulence while others do not. More details may be found in Das and Arakeri [33].

There is uncertainty about the exact α at which the inflection point of stability curves occurs, although those of Sarpkaya [34] and Stettler and Hussain [35] have almost a similar turn at α = 6 to 7. It seems there is another inflection stability point at higher α if $A \geq 1$. Due to the lack of available data on experimental results, it is not clear where the peak of the critical curve is at high pulsation ratios. The experimental results of [32] appear to be close to those of the current theory, although they were achieved with different Womersely numbers. There is a major gap in the predictions of all results and those of Floquet theory, which was found difficult to apply at higher pulsation ratios [10]. By utilizing the quasi-steady approach, the effect of Hartmann (Ha) and Womersley (α) numbers on the flow transition is determined via exact numbers of Re_c as shown in Fig. 6. The flow tends to be stable if $\alpha < 19$ under the magnetic field effect, mostly due to the Richardson's annular effect, where the boundary layer thickness is relatively big to that of high oscillation ([18]). That means the stability can be improved by increasing the Hartmann number if $\alpha < 19$. All flow conditions

show the same critical Reynolds number at $\alpha = 19$ regardless of the Hartmann number (*Ha*). That indicates the deflection point is located here when the magnetic environment is available. On the contrary, when $\alpha > 19$, the flow seems to be unstable, and the Re_c decreases with *Ha*. While previous related data have not been found, several numerical results obtained from the current direct numerical simulations presented next, confirm this flow behavior under the magnetic field influence.

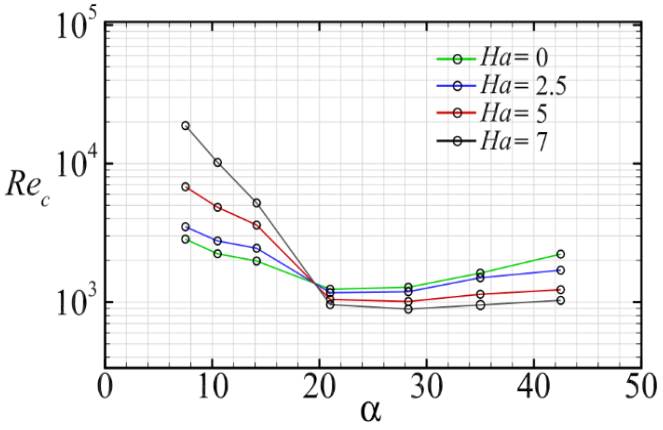

Fig. 6. Critical Reynolds numbers predicted by the quasi-steady method under the influence of magnetic field for different Hartmann numbers.

5.5. Wall effect

The wall effect on flow stability was investigated using two-dimensional simulations with $Re = 1500$, $\alpha = 28.29$ and $Ha = 0$, at which the flow was predicted to be unstable theoretically. However, the flow appears to be laminar when no disturbances are promoted in the smooth pipe. The flow becomes unstable when an external influence is applied, and this is in some way compatible with the results of the current linear theory. The stability was examined for some scenarios that may the pulsatile flow commonly undergoes. The waviness of the wall with $\varepsilon = 0.001$ was incorporated as well as 75% reduction area. The flow instability can be declared according to some fluctuations appear in the pathlines of the axial velocity. These flow patterns can interpret some aspects of vortex and turbulence that are usually formed at some distance from the throat.

The velocity profiles at three radial positions ($r = 0$, 0.3 and 0.49) in Fig. 7(a) and (b) for the smooth and 0.001-ε rough pipe, respectively, seem to be identical at $x = 14$, the farthest location post the blockage in the domain. Figures 7(c) and (d) show the wall shear stresses in the pipe at $x = 2$, 5, and 14, which correspond to the velocities in Figs. 7(a) and (b). Figure 7(c) depicts a smooth pulsatile flow, as opposed to Fig. 7 (d), where the values are higher, and the flow is more disturbed. It is known that the nonlinear disturbances created by the wall roughness can drive the flow to unstable zone at lower flow conditions than what those imposed for the smooth pipe.

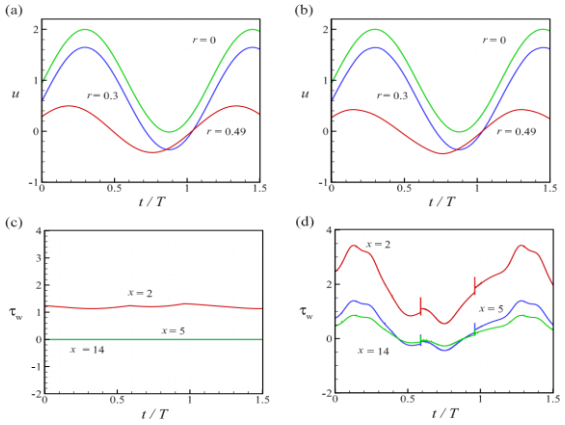

Fig. 7. Axial velocities and wall shear stresses at various radial and axial positions for a flat domain that is: (a) and (c) smooth, (b) and (d) rough with a height of 0.001.

5.6. Magnetic field effect

The transverse magnetic field with a flux B^* was applied on the entire pipe at flow conditions of Re and $\mathrm{Re_m}$ = 2500 and 200, respectively, where Re_m is the magnetic Reynolds number, or $Re_m = \hat{u}^* R^* / \zeta^*$, where ζ^* is the magnetic diffusivity. Increasing the Hartmann number from 0 to 7 suppressed the fluctuations at α = 14.14, which was considered relatively small with respect to the deflection point seen in Fig. 6. To illustrate further the effect of *Ha*, the wall shear stress profiles are shown in the left corner of Fig. 8. The results of τ_w were taken at the distance from x = 5.8 to 6 of the rough pipe flow.

Velocity overshoots with some fluctuations highly occur near the wall in the case of α = 42.5, see Figs. 8(c) and (d). The velocity profiles change everywhere in the pipe, and the wall shear stress encounters sudden increases. Turbulence is anticipated to develop at some distance following the pipe reduction zone when the Reynolds number is rather higher. As the Hartmann number rises, the velocity gradients increase, as previously noted, and the flow becomes unstable as a result of the produced perturbations. The flow tends to be more sensitive to disturbances at these flow conditions, so that it becomes unstable at lower Reynolds numbers as shown in Fig. 6 when the Hartmann number is high.

As the Womersley number changes from 14.14 to 42.5, the flow experiences overshooting event near the walls, as indicated in Fig. 9. Likewise, the influence of magnetic field at a fixed Womersley number steers the flow towards the walls. With α having a value of 19 or less, the flow becomes more stable and wall clustered as the magnetic field increases. This phenomena resembles the idea of impedance in some ways, where the flow, periodic pressure gradient, viscosity, and magnetic field can be viewed as the system's mass, cyclic spring force, and dampers. The equation of Lee et al. [36] for impedance may have been used if the walls were thought of as elastic in this context. For computational analysis, Fig. 10 demonstrates the influence of magnetic environment surrounding the entire pipe in terms of Womersley number at Re = 2500 and $\mathrm{Re_m}$ = 200. The boundary conditions for the magnetic field are the same type (Dirichlet) as for the velocity

field at the pipe ends. As an inlet condition, the analytical solution described in Eq. (6) was employed, where the magnetic field does not change across the flat pipe. At α = 14.14 and 42.5, the relation of Womersley and Hartmann numbers with magnetic field flux is shown for $Ha = 0$ and 7. If the α is significant compared to small oscillations, the magnetism has a big influence. The contour depicts the magnetic effect varying with the area reduction. The magnetic effect (B^*) is intensified at the throttle zone while Ha and other fluid parameters are maintained.

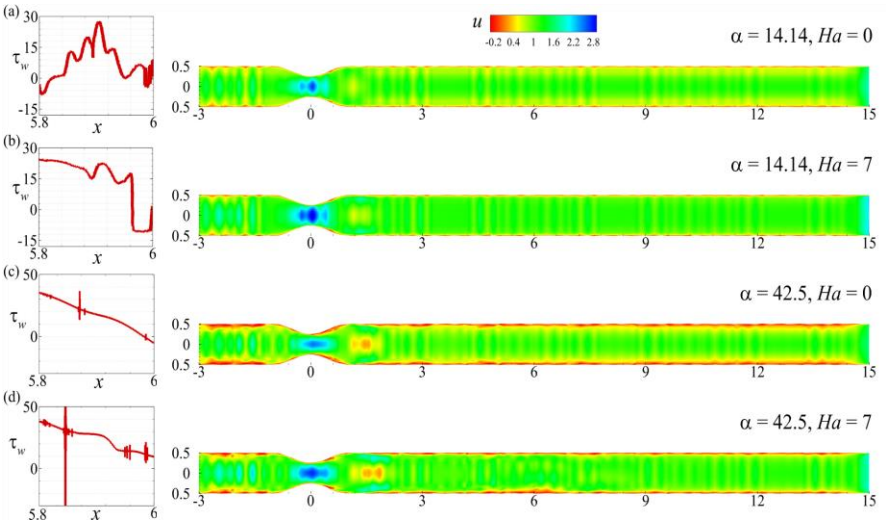

Fig. 8. Effect of magnetic field on a pipe flow of 75% constricted area with roughness height of 0.001. The wall shear stresses and the contour plots of axial velocity are examined at Re **= 2500, Re$_m$ = 200 and t/T= 3⁄8 with Ha = 0 and 7 for: (a) and (b) α = 14.14, (c) and (d) α = 42.5.**

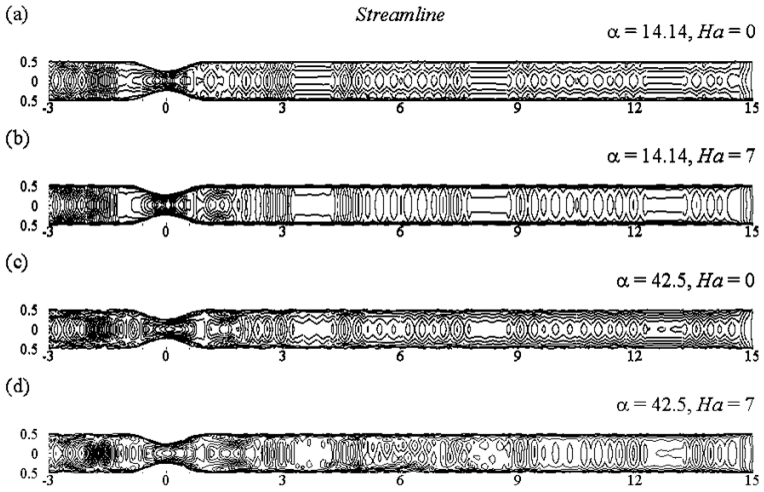

Fig. 9. Streamlines of a pipe flow of 75% constricted area with roughness height of 0.001 are examined at Re **= 2500, Re$_m$ = 200 and t/T= 3⁄8 with Ha = 0 and 7 for: (a) and (b) α = 14.14, (c) and (d) α = 42.5.**

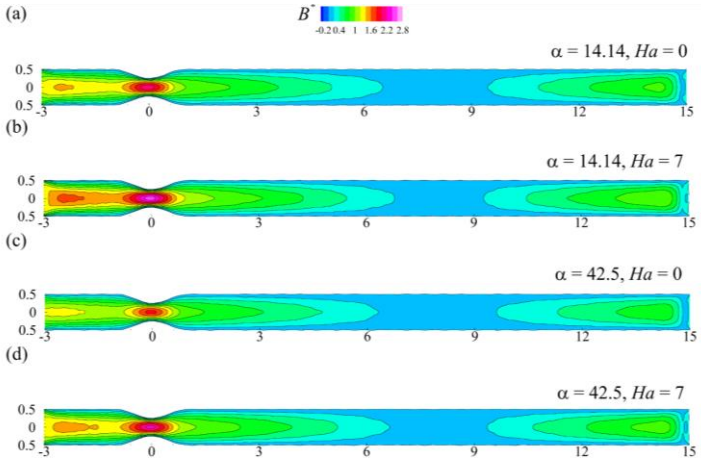

Fig. 10. Contour plots of magnetic field (Tesla), applied on a pipe flow of 75% constricted area with roughness height of 0.001, are examined at Re = 2500, Re_m **= 200 and** $t/T = 3/8$ **with** Ha **= 0 and 7 for: (a) and (b)** α **= 14.14, (c) and (d)** α **= 42.5.**

6. Conclusions

The induced force dampens unsteady velocity profiles inside a magnetic environment, whereas velocity derivatives at the wall and reduced area are enhanced. Two-dimensional disturbances for this type of flow can be triggered by the configuration of wall and operating conditions. The assumptions of the quasi-steady technique described herein seem to be effective in identifying transition thresholds. This is confirmed by the numerical solution of the initial value problem and other data from prior studies, although the pulsation ratio is taken one only and the precise exact transition zones cannot be identified from the literature. Nevertheless, applying a transverse magnetic field has a stabilized effect on the pulsatile flow when the Womersley number is ≤ 19 while the opposite is true for higher oscillations. If the perturbations are axisymmetric, the flow will be laminar and not fluctuated anywhere downstream the flow, as noticed in other studies, but some fluctuations can grow if Hartmann and Womersley numbers are significantly high. Also, the influence of wall roughness should be considered whether or not the flow passes through a throat. Since the evaluated eigenvalues are the highest growth rate at each instant of time, where the base flow is considered frozen, it is anticipated that the current theory will hold true for a variety of pulsing flow types with high Womersley numbers.

Nomenclatures

A	Pulsation ratio, $\hat{u}_o^* / \hat{u}_s^*$
B^*	Dimensional Magnetic field flux, Tesla (T)
c	Dimensionless velocity of disturbance waves
D^*	Dimensional pipe diameter, m
E	Number of elements
f_1, f_2	Functions used for wall modifications
I_0	Modified Bessel function of the first kind

$Im[\omega]$	Imaginary part of eigenvalues, disturbance growth rate
J_0	Bessel function of the first kind
k	Dimensionless wave number
N	Lagrange polynomial degree
$p*$	Dimensional static pressure, N/m^2
R^*	Dimensional pipe radius, m
$\mathbb{R}$	Real part
r	Radial coordinate nondimensionalized by R^*
T	Dimensionless period of flow oscillation
t	Dimensionless time
U	Axial laminar velocity normalized by $\hat{u}^*$
u	Instantaneous axial velocity normalized by $\hat{u}^*$
$\hat{u}^*$	Dimensional axial velocity amplitude at r = 0, $\hat{u}^* = \hat{u}_s^* + \hat{u}_o^*$, m
^{u}rms	Root-mean-square velocity nondimensionalized by $\hat{u}^*$

Greek Symbols

υ	Dimensional radial velocity normalized by $\hat{u}^*$
ψ^*	Dimensional stream function, kg/m s
x	Dimensionless axial coordinate nondimensionalized by R^*
η	Disturbance amplitude function.
δ	Dimensionless throat amplitude
ϕ	Dimensionless function
ι	Roughness parameter normalized by R^*
σ^*	Electrical conductivity, S/m (siemens per meter)
ε	Dimensionless roughness amplitude defined as ε^*/R^*
ν^*	Kinematic viscosity, m^2 s^{-1}
μ^*	Dynamic viscosity, Pa s
Ω	Angular frequency nondimensionalized by $\hat{u}^*/R^*$
Ψ	Stream function for the base flow nondimensionalized by $\hat{u}^*/R^*$
ψ	Stream function for the disturbances nondimensionalized by $\hat{u}^*/R^*$
ρ^*	Fluid density, kg/m^3
τ_w	Dimensionless wall shear stress nondimensionalized by $\rho^*\hat{u}^{*2}$
ω	Eigenvalue indicating growth rate of disturbance
ζ^*	Magnetic diffusivity, m²/s
$\Re(\boldsymbol{u})$	Normalized residual of the vector velocity (**u**)

Dimensionless numbers

Ha	Hartmann number, Ha $= B^*R^*\sqrt{\sigma^*/\mu^*}$
Re	Reynolds number based on $\hat{u}^*$and R^*, Re $= \hat{u}^*R^*/\nu^*$
$\mathrm{Re_c}$	Critical Reynolds number based on $\hat{u}^*$and R^{**}
$\mathrm{Re_m}$	Magnetic Reynolds number, $\hat{u}^*R^*/\zeta^*$
α	Womersley number, $R^*\sqrt{\Omega^*/\nu^*}$

References

1. Nabavi, M.; and Siddiqui, K. (2010). A critical review on advanced velocity measurement techniques in pulsating flows. *Measurement Science and Technology*, 21(4), 04200.
2. Misra, J.; and Shit, G.C. (2007). Effect of magnetic field on blood flow through an artery: A numerical model. *Journal of Computational Technologies*, 12(4), 3-16.
3. Parida, M. (2017). Study of MHD flow of blood with heat transfer in an arterial segment under the effect of periodic body acceleration. *International Journal of Applied Mathematics*, 30(4).
4. Rashidi, S.; Esfahani, J.A.; and Maskaniyan, M. (2017). Applications of magnetohydrodynamics in biological systems-a review on the numerical studies. *Journal of Magnetism and Magnetic Materials*, 439, 358-372.
5. Sharma, M.K.; Bansal, K.; and Bansal, S. (2012). Pulsatile unsteady flow of blood through porous medium in a stenotic artery under the influence of transverse magnetic field. *Korea-Australia Rheology Journal*, 24(3), 181-189.
6. Khechiba, A.; Benakcha, Y.; Ghezal, A.; and Spetiri, P. (2018). Combined MHD and pulsatile flow on porous medium. *Fluid Dynamics & Materials Processing*, 14(2), 137-154.
7. Camobreco, C.J.; Pothérat, A.; and Sheard, G.J. (2021). Stability of pulsatile quasi-two-dimensional duct flows under a transverse magnetic field. *Physical Review Fluids*, 6(5), 053903.
8. Bandyopadhyay, S.; and Layek, G.C. (2012). Study of magnetohydrodynamic pulsatile flow in a constricted channel. *Communications in Nonlinear Science and Numerical Simulation*, 17(6), 2434-2446.
9. Kiran, G.R.; Murthy, V.R.; and Krishnamacharya, G.R. (2019). Pulsatile flow of a dusty fluid thorough a constricted channel in the presence of magnetic field. *Materials Today*: *Proceedings*, 19, 2645-2649.
10. Thomas, C.; Bassom, A.P.; Blennerhassett, P.J.; and Davies, C. (2011). The linear stability of oscillatory Poiseuille flow in channels and pipes. *Proceedings of the Royal Society A*: *Mathematical, Physical and Engineering Sciences*, 467(2133), 2643-2662.
11. Sadrizadeh, S. (2012). *Instabilities in pulsating pipe flow of shear-thinning and shear-thickening fluids*. Degree Project. Department of Management and Engineering Linköping University, Sweden.
12. Fedele, F.; Hitt, D.L.; and Prabhu, R.D. (2005). Revisiting the stability of pulsatile pipe flow. *European Journal of Mechanics - B/Fluids*, 24(2), 237-254.
13. Pier, B.; and Schmid, P.J. (2017). Linear and nonlinear dynamics of pulsatile channel flow. *Journal of Fluid Mechanics*, 815, 435-480.
14. Xu, D.; and Avila, M. (2018). The effect of pulsation frequency on transition in pulsatile pipe flow. *Journal of Fluid Mechanics*, 857, 937-951.
15. Varghese, S.; Frankel, S.; and Fischer, P. (2007). Direct numerical simulation of stenotic flows. Part 2. pulsatile flow. *Journal of Fluid Mechanics*, 582, 281-318.
16. Sherwin, S.J.; and Blackburn, H.M. (2005). Three-dimensional instabilities and transition of steady and pulsatile axisymmetric stenotic flows. *Journal of Fluid Mechanics*, 533.

17. Xu, D.; Warnecke, S.; Song, B.; Ma, X.; and Hof, B. (2017). Transition to turbulence in pulsating pipe flow. *Journal of Fluid Mechanics*, 831, 418-432.
18. Lee, Y; and Abdulrasool, A.A. (2018). Comparison between theories and experiments in transition of purely oscillating pipe flow. *Proceedings of the* 2018 *Fluid Dynamics Conference*. American Institute of Aeronautics and Astronautics, Atlanta, Georgia.
19. Griffith, M.D.; Leweke, T.; Thompson, M.C.; and Hourigan, K. (2009). Pulsatile flow in stenotic geometries: flow behaviour and stability. *Journal of Fluid Mechanics*, 622, 291-320.
20. Abdulrasool, A.A. (2020). *Theoretical and computational analyses on transition and turbulence in purely oscillating pipe flow*. Doctoral Dissertations and Master's Theses. 511. Mechanical Engineering Department, Embry-Riddle Aeronautical University, Florida-32114, USA.
21. Farrokhi, H.; Otuya, D.O.; Khimchenko, A.; and Dong, J. (2020). *Magnetohydrodynamics in biomedical applications*. Nanofluid Flow in Porous Media. IntechOpen.
22. Womersley, J.R. (1955). Method for the calculation of velocity, rate of flow and viscous drag in arteries when the pressure gradient is known. *The Journal of Physiology*, 127(3), 553-563.
23. Ray, S.; Ünsal, B.; Durst, F.; Ertunc, Ö.; and Bayoumi, O.A. (2005). Mass flow rate controlled fully developed laminar pulsating pipe flows. *Journal of Fluids Engineering*, 127(3), 405-418.
24. Ha, H.; Lantz, J.; Ziegler, M.; Casas, B.; Karlsson, M.; Dyverfeldt, P.; and Ebbers, T. (2017). Estimating the irreversible pressure drop across a stenosis by quantifying turbulence production using 4D flow MRI. *Scientific Reports*, 7(1), 46618.
25. ÇarpinlioÇğlu, M.Ö.; and GündoÇğdu, M.Y. (2001). A critical review on pulsatile pipe flow studies directing towards future research topics. *Flow Measurement and Instrumentation*, 12(3),163-174.
26. Hairer, E.; Wanner, G.; and Lubich, C. (2006). *Geometric numerical integration*. Springer Series in Computational Mathematics (SSCM, volume 31).
27. Singer, B.A.; Ferziger, J.H.; and Reed, H.L. (1989). Numerical simulations of transition in oscillatory plane channel flow. *Journal of Fluid Mechanics*, 208, 45-66.
28. Fischer, P.F.; Kruse, G.W.; and Loth, F. (2002). Spectral element methods for transitional flows in complex geometries. *Journal of Scientific Computing*, 17(1/4), 81-98.
29. Abdulrasool, A.A.; and Lee, Y. (2019). A DNS study on roughness-induced transition in oscillating pipe flow by employing overset methodology. *Proceedings of the ASME* 2019 *International Mechanical Engineering Congress and Exposition*, Salt Lake City, Utah, USA, V007T08A022.
30. Bauer, A.; Wegt, S.; Bopp, M.; Jakirlic, S.; Tropea, C.; Krafft, A.J.; Shokina, N.; Hennig, J.; Teschner, G.; and Egger, H. (2019). Comparison of wall shear stress estimates obtained by laser doppler velocimetry, magnetic resonance imaging and numerical simulations. *Experiments in Fluids*, 60(7), 112.

31. Çarpinlioğlu, M.Ö.; and GündoÇğdu, M.Y. (2001). A critical review on pulsatile pipe flow studies directing towards future research topics. *Flow Measurement and Instrumentation*, 12(3),163-174.
32. Lodahal, C.R.; Sumer, B.M.; and FredsØe, J. (1998). Turbulent combined oscillatory flow and current in a pipe. *Journal of Fluid Mechanics*, 373, 313-348.
33. Das, D.; and Arakeri, J.H. (1998). Transition of unsteady velocity profiles with reverse flow. *Journal of Fluid Mechanics*, 374, 251-283.
34. Sarpkaya, T. (1966). Experimental determination of the critical Reynolds number for pulsating Poiseuille flow. *Journal of Basic Engineering*, 88(3), 589-598.
35. Stettler, J.C.; and Hussain, A.K.M.F. (1986). On transition of the pulsatile pipe flow. *Journal of Fluid Mechanics*, 170,169-197.
36. Lee, V.C.; Abakr, Y.A.; and Woo, K.C. (2015). Dynamics of fluid in oscillatory flow: The Z-component. *Journal of Engineering Science and Technology*, 10(10),1361-1371.

Appendix A

A. Derivation of the Analytical Solution (Eq. 6)

When a magnetic field ($\vec{B}^*$) is imposed on a moving conductive fluid, electrical currents with intensity $\vec{J}^*$ can be induced. Electromagnetic force, or Lorentz force ($\vec{F}_m^*$), will be created due to the interaction of the current lines with the magnetic field flux. This force is perpendicular on both $\vec{B}^*$ and $\vec{J}^*$ according to the right-hand rule. Mathematically, if the current density is considered as

$$\vec{J}^* = \sigma^*(\vec{E}^* + \vec{u}^* \times \vec{B}^*),$$

where σ^* is the electrical conductivity, E^* is the electrical field (neglected in this study), u^* is the axial fluid velocity, the electromagnetic force in the axial direction will be

$$\vec{F}_m^* = \vec{J}^* \times \vec{B}^* = \sigma^*(\vec{u}^* \times \vec{B}^*) \times \vec{B}^*.$$

Note that the uniform magnetic field, $\vec{B}^* = B_{x^*}^* \vec{e}_{x^*} + B_{r^*}^* \vec{e}_{r^*}$ of a constant magnitude B^*, is considered in this study, where $\vec{e}_{x^*}$ and $\vec{e}_{r^*}$ are unit vectors in cylindrical coordinates. The magnetic field is in a transverse direction to both the $\vec{F}_m^*$ and $\vec{u}^*$, which are in turn opposite to each other. The $\vec{B}^*$ is constant over the entire pipe but still changes with the pipe radius (R^*) if there is a throat. Thus, the momentum equation involving $\vec{F}_m^*$ for a fully developed laminar flow of incompressible fluid inside a flat pipe is

$$\frac{\partial u^*}{\partial t^*} = -\frac{1}{\rho^*}\frac{\partial p^*}{\partial x^*} - \frac{\sigma^* B^{*2}}{\rho^*} u^* + \frac{\mu^*}{\rho^*}\left(\frac{\partial^2 u^*}{\partial r^{*2}} + \frac{1}{r^*}\frac{\partial u^*}{\partial r^*}\right), \quad (18)$$

where $-\partial p^*/\partial x^* = \sum_{n=0}^{M} \Lambda_n^* e^{i\Omega^* n t^*}$ at which n represents the number of harmonics and M is theoretically infinite. The boundary conditions are axisymmetry at the centre and no-slip condition on the wall. An analytical solution for this non-homogeneous second order partial differential equation is obtained via

decomposing the flow into steady (u_s^*) and unsteady (or oscillatory u_o^*) components, i.e.,

$u^* = u_s^* + u_o^*$.

A.1. Steady Component

In the steady case, where $-\partial p^*/\partial x^* = \Lambda_0^*$, the governing equation turns into non-homogeneous second order ordinary differential equation, or

$$\frac{\partial^2 u^*}{\partial r^{*2}} + \frac{1}{r^*}\frac{\partial u^*}{\partial r^*} - \frac{\sigma^* B^{*2}}{\mu^*} u^* = -\frac{\Lambda_0^*}{\mu^*}, \tag{19}$$

and the general solution consists of two superposition solution parts (homogeneous and non-homogeneous), i.e.,

$$u_s^* = C_1 I_0\left(\sqrt{\frac{\sigma^* B^{*2}}{\mu^*}} r^*\right) + C_2 K_0\left(\sqrt{\frac{\sigma^* B^{*2}}{\mu^*}} r^*\right) + \frac{\Lambda_0^*}{\sigma^* B^{*2}}. \tag{20}$$

The boundary condition at the axis of symmetry forces $C_2 = 0$, so the solution for steady flow is

$$u_s^* = \frac{\Lambda_0^*}{\sigma^* B^{*2}}\left(1 - \frac{I_0(Ha \cdot r)}{I_0(Ha)}\right), \tag{21}$$

where $Ha = B^* R^* \sqrt{\sigma^*/\mu^*}$.

A.2. Unsteady Component

If $-\partial p^*/\partial x^* = \Lambda_1^* e^{i\Omega^* t^*}$ drives the flow, the axial velocity and its derivatives turn into

$u_o^* = f^* e^{i\Omega^* t^*}$,

$\frac{du_o^*}{dr^*} = \frac{df^*}{dr^*} e^{i\Omega^* t^*}$,

$\frac{d^2 u_o^*}{dr^{*2}} = \frac{d^2 f^*}{dr^{*2}} e^{i\Omega^* t^*}$,

$\frac{du_o^*}{dt^*} = i\Omega^* f^* e^{i\Omega^* t^*}$,

that Eq. (18) can be converted to

$$\frac{\partial^2 f^*}{\partial r^{*2}} + \frac{1}{r^*}\frac{\partial f^*}{\partial r^*} - \left(\frac{\sigma^* B^{*2}}{\mu^*} + i\frac{\Omega^*}{\nu^*}\right) f^* = -\frac{\Lambda_1^*}{\mu^*}, \text{ or} \tag{22}$$

$$\frac{\partial^2 f^*}{\partial r^{*2}} + \frac{1}{r^*}\frac{\partial f^*}{\partial r^*} - \gamma^* f^* = -\frac{\Lambda_1^*}{\mu^*}. \tag{23}$$

The general solution of such equation can be sought by

$$f^* = C_3 I_0(\sqrt{\gamma^*} \cdot r^*) + C_4 K_0(\sqrt{\gamma^*} \cdot r^*) + \frac{\Lambda_1^*}{\gamma^* \mu^*}, \tag{24}$$

where $\gamma^* = \frac{\sigma^* B^{*2}}{\mu^*} + i\frac{\Omega^*}{\nu^*}$, $\gamma = \sqrt{\gamma^*} R^*$, $\gamma = \sqrt{Ha^2 + i\alpha^2}$ and $\alpha = R^* \sqrt{\Omega^*/\nu^*}$. Based on these changes and the boundary condition at the axis of symmetry, where $C_4 = 0$, the solution is

$$u_o^* = f^* e^{i\Omega^* t^*} = \frac{\Lambda_1^*}{\gamma^* \mu^*}\left(1 - \frac{I_0(\gamma \cdot r)}{I_0(\gamma)}\right) e^{i\Omega^* t^*}. \quad (25)$$

The pulsatile flow velocity is obtained by combining the two component solutions as follows:

$$u^* = \frac{\Lambda_0^*}{\sigma^* B^{*2}}\left(1 - \frac{I_0(Ha \cdot r)}{I_0(Ha)}\right) + \frac{\Lambda_1^*}{\gamma^* \mu^*}\left(1 - \frac{I_0(\gamma \cdot r)}{I_0(\gamma)}\right) e^{i\Omega^* t^*}. \quad (26)$$

Finally, the normalized velocity for the current analysis, $U(r,t)$ with respect to $\hat{u}^*$, is

$$U(r,t) = \left|\frac{I_0(Ha)}{I_0(Ha)-1}\right|\left(1 - \frac{I_0(Ha \cdot r)}{I_0(Ha)}\right) + \left|\frac{I_0(\gamma)}{I_0(\gamma)-1}\right| \cdot \mathbb{R}\left[\left(1 - \frac{I_0(\gamma \cdot r)}{I_0(\gamma)}\right) \cdot \frac{e^{i\Omega t}}{i}\right], \quad (27)$$

where the amplitudes for each component are

$$\left|\frac{I_0(Ha)}{I_0(Ha) - 1}\right| \equiv \frac{Re}{Ha^2} \Lambda_0, \text{and}$$

$$\left|\frac{I_0(\gamma)}{I_0(\gamma) - 1}\right| \equiv \frac{Re}{i\gamma^2} \Lambda_1.$$